Applied Radiation and Isotopes 218 (2025) 111693

Contents lists available at ScienceDirect

Applied Radiation and Isotopes

journal homepage: www.elsevier.com/locate/apradiso

Ion implantation of the electron-capture nuclide ^{55}Fe for measurements by means of metallic microcalorimeters

Thorben Niemeyer [a,*], Daniel Mowitz [a], Sebastian Berndt [a,b], Jörn Beyer [c], Holger Dorrer [b], Christoph E. Düllmann [b,d,e], Alexander Göggelmann [f], Raphael Hasse [a], Sebastian Kempf [h], Tom Kieck [d,e], Nina Kneip [a], Karsten Kossert [f], Andrea T. Loria Basto [b,e], Christoph Mokry [b], Michael Müller [g], Ole J. Nähle [f], Dennis Renisch [b,e], Jörg Runke [b], Dominik Studer [d], Marcell P. Takács [f], Klaus Wendt [a]

[a] Johannes-Gutenberg-Universität Mainz, Institut für Physik, Staudingerweg 7, 55128, Mainz, Germany
[b] Johannes-Gutenberg-Universität Mainz, Department Chemie – Standort TRIGA, Fritz-Straßmann-Weg 2, 55128, Mainz, Germany
[c] Physikalisch-Technische Bundesanstalt, Abbestraße 2–12, 10587 Berlin, Germany
[d] GSI Helmholtzzentrum für Schwerionenforschung, Planckstraße 1, 64291, Darmstadt, Germany
[e] Helmholtz Institut Mainz, Staudingerweg 18, 55128, Mainz, Germany
[f] Physikalisch-Technische Bundesanstalt (PTB), Bundesallee 100, 38116, Braunschweig, Germany
[g] Institute of Micro- and Nanoelectronic Systems (IMS), Karlsruhe Institute of Technology (KIT), Hertzstrasse 16, 76187, Karlsruhe, Germany
[h] Institute for Data Processing and Electronics (IPE), Karlsruhe Institute of Technology (KIT), Hermann-von-Helmholtz-Platz 1, 76344, Karlsruhe, Germany

A B S T R A C T

Precise measurements of fundamental decay data such as energies and transition probabilities of radioactive isotopes are important for the development of corresponding nuclear modelling, activity determination and various applications in science and technology. The EMPIR project PrimA-LTD -"Towards new Primary Activity standardisation methods based on Low-Temperature Detectors" - aims to measure the electron-capture decay of ^{55}Fe very precisely using Metallic Microcalorimeters (MMCs) with outstandingly high energy resolution. Using a high-statistics measurement, electron-capture probabilities shall be precisely determined and higher-order effects such as electron shake-up and shake-off shall be examined with unprecedented precision. A key to success for this project is sample preparation. This work reports on the implantation of ^{55}Fe into the 140 μm × 140 μm gold absorbers of the MMCs as a proof of principle for scalability. Building up on preparatory laser-spectroscopic studies on stable ^{56}Fe, laser resonance ionization at the RISIKO mass separator was used to produce a monoisotopic ^{55}Fe ion beam with the required specifications. Successful implantations of this isotope (i) into 32 test absorbers with about 0.7(2) Bq each and (ii) into various on-chip absorbers with an activity close to the requested 5 Bq per absorber are presented. The impact of the implantation on the quality of spectra is highlighted on the basis of first MMC test measurements.

1. Introduction

The knowledge of nuclear decay properties such as half-lives, energies and emission probabilities is essential for various applications in science, nuclear medicine, and industry (see, e.g., - Pommé, 2022). In recent years, several papers have highlighted the importance of beta spectra for determining the activity (see, e.g., Kossert et al., 2011; Kossert and Mougeot, 2015; Kossert et al., 2018; Kossert and Mougeot, 2021; Bobin et al., 2023) and significant progress has been made with new experiments using Metallic Microcalorimeters (MMCs), which offer high energy resolution and a low detection threshold (Rotzinger et al., 2008; Loidl et al., 2010, 2014; Kossert et al., 2022; Paulsen et al., 2024). The corresponding work has contributed to the fact that theoretical calculation models are much more advanced today (Mougeot, 2023 and references therein). The situation is similar for electron-capture nuclides like ^{55}Fe. In radionuclide metrology, the activity of ^{55}Fe is mostly determined by the TDCR (Triple-to-Double Coincidence Counting) method based on liquid scintillation counting (Broda et al., 2007; Kossert et al., 2015) and the results depend much on the fractional electron-capture probabilities (Broda et al., 2021). Again, MMCs have proven useful for experimental determination, although it is desirable to improve the precision achieved in a pioneering experiment (Loidl et al., 2018). In addition to determining electron-capture probabilities, there is also a great need to better understand the electron-capture process with

* Corresponding author.
E-mail address: tniemey@uni-mainz.de (T. Niemeyer).

https://doi.org/10.1016/j.apradiso.2025.111693
Received 31 May 2024; Received in revised form 25 November 2024; Accepted 19 January 2025
Available online 27 January 2025

its subsequent atomic shell rearrangement. Precise data are needed to develop enhanced models for higher order effects such as electron shake-up and shake-off. One objective of the EMPIR project PrimA-LTD (PrimA-LTD) is accurate MMC measurements of ^{55}Fe electron capture spectra, which are divided into two parts:

- the energy range from 50 eV to 6600 eV to measure the M-shell, L-subshell and K-shell electron-capture probabilities, and to observe the shake-up contribution and shake-off below 6 keV
- the energy range from 0.50 keV to 231 keV to observe shake-off above 6 keV.

This results in two essential requirements: The spectrum must be of excellent quality so that relevant peaks can be reliably resolved, and the measurements must be carried out with very high statistics. The first condition can best be met if samples are prepared using ion implantation. Since MMCs can only measure small activities due to long signal decay times in the range of a few milliseconds and associated problems with pile-up, the measurement must be carried out simultaneously in several detector pixels in order to reduce the total duration of an experiment. These requirements are comparable to those of the ECHo experiment which uses the electron capture of ^{163}Ho to constrain the neutrino mass (Gastaldo et al., 2017).

A well-suited technology for placing the radioactive source in the specific detector-assemblies of MMCs is implantation at an ion beam facility, e.g., an isotope separator facility. Highest purity of the implanted sample combined with high overall efficiency in the transfer of the possibly rare or even highly precious isotope is achieved by using the specific ionization process of Resonance Ionization Mass Spectrometry (RIMS). This type of radioactive source preparation has been demonstrated in corresponding isotope collections at the RISIKO off-line mass separator facility for radioisotopes, operated at Mainz University, namely via implantation of ^{163}Ho for the ECHo collaboration (Kieck et al., 2019), ^{53}Mn with a related separation from ^{54}Mn (Kneip et al., 2022), ^{226}Ra (Mertes et al., 2022), ^{157}Tb with a related separation from ^{158}Tb (Studer et al., 2024; Riffaud et al., 2024) in MMCs and other targets.

This paper reports on the first production of pure samples of the widely-used electron-capture nuclide ^{55}Fe by means of ion implantation. The preparatory laser spectroscopy in the neutral spectrum of iron will be presented elsewhere, while the subsequent successful implantation of well-defined atom numbers into the gold absorbers of specific MMCs via RIMS at the RISIKO laser mass separator facility of Mainz University is discussed here.

2. Experimental details

Laser Resonance Ionization takes advantage of the element-specific energy levels of the atom, allowing for highly selective as well as highly efficient ionization by successive excitation along strong optical transitions. The laser system used in Mainz for efficient and selective ionization of iron atoms consists of pulsed tuneable titanium:sapphire (Ti:Sa) lasers, involving two slightly different types of the so-called standard (Grüning et al., 2004; Mattolat et al., 2009) as well as the grating-assisted resonator design (Teigelhöfer et al., 2010). Each Ti:Sa laser is optically pumped by a commercial high power frequency doubled Nd:YAG laser at 532 nm with about 14 W pump power per laser medium and 10 kHz pulse repetition rate. The spectral range of these Ti:Sa lasers covers 680–950 nm with a spectral line width in the order of 2–5 GHz. Frequency doubling and tripling is applied to extend this range into the additional range of 450 nm down to 220 nm. The individual Ti:Sa laser beams are guided to overlap within the source region of the RISIKO mass separator, as depicted schematically in Fig. 1. For the investigations discussed here the following components of RISIKO were used: the sample material is introduced into a resistively heated atomizer cavity of 35 mm length and 2.5 mm diameter, which is gradually heated up to about 2300 K. Sample atoms are smoothly evaporated, resonantly ionized by the laser radiation in a multi-step process and resulting ions are guided by field penetration of the extraction potential towards the exit hole of the atomizer. Application of a high voltage potential of 30 kV to the ion source leads to two-step electrostatic acceleration via an extractor electrode into the mass spectrometer. Ion extraction and beam formation is performed by ion optics consisting of an Einzel lens, typically set to approx. 9.6 kV, horizontal and vertical ion deflectors and a quadrupole triplet for optimally shaping a parallel beam. A 60° sector field magnet with 1 m focal length and a narrow slit of typically 1 mm width in the focal plane serve for mass separation with a resolution of $\frac{m}{\Delta m} \approx 800$ (Kneip et al., 2022). A retractable Faraday cup (FC1) is used for ion current control during the implantation process. Post focalization by another Einzel lens set to ≈12.5 kV and a computer-controlled deflector system, both installed behind the slit system, see Fig. 1, directs the highly focused ion beam of typically 0.5 mm diameter precisely into the MMC absorbers and allows for automated scanning of the ion beam via the deflector voltages at the post-focalization stage across a predefined implantation area. The collector, i.e., the MMC chip, is placed within a Faraday cup for read out of the implantation current and in this way absolute determination of the implanted ion number.

The detector chip design was developed at Karlsruhe Institute of Technology (KIT), Karlsruhe, Germany, and is described in detail in (Müller et al., 2024). A detailed layout is visualized in Fig. 9 for the implanted area while Fig. 10a shows the absorbers in detail. Here, we briefly outline the parameters relevant for implantation. Every MMC pixel has a 0.17 × 0.17 mm^2 gold absorber area of 12 µm thickness, on which an area of precisely 0.136 × 0.136 mm^2 is accessible for implantation while the rest of the chip is either placed behind the slit aperture or covered with photoresist preventing parasitic implantation. There are 32 individual MMC pixels on each chip arranged with some spatial separation in 4 blocks of 8 along a line, which spreads out to 20 mm overall length including three large gaps of up to 2 mm widths, see (Müller et al., 2024) for further details. For each MMC chip a loading with 5 Bq of ^{55}Fe is envisaged. The total activity of 160 Bq on all 32 pixels corresponds to $2{\cdot}10^{10}$ ions to be implanted into the active pixels, which is a very low number, while considerable losses must be considered arising from the rather low geometrical efficiency of hitting the very small MMC pixels with the macroscopic ion beam size. The overall

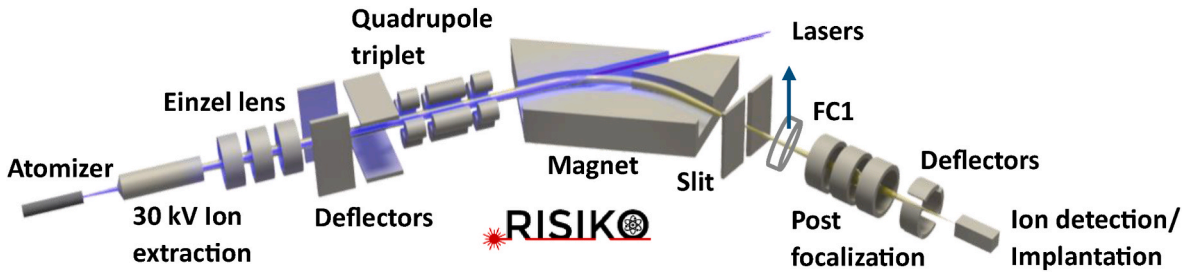

Fig. 1. Schematics of the RISIKO mass separator. Faraday-cup 1 (FC1) can be retraced during implantation. For a detailed description see text.

area as addressed for implantation amounts to 20 mm length x 1 mm widths, corresponding to an area of 20 mm^2, with an actual active MMC pixel area of only 32 × 0.136 mm x 0.136 mm ≈ 0.6 mm^2. Correspondingly, even under optimum focussing and pointing only 3 % of the ion beam is implanted into the MMC pixels. Correspondingly, a total number of implanted ions of about 10^{12} must be foreseen per chip. This number does not yet consider ionization probability and mass separator transmission, which increases the necessary ion number by a further factor of 10–30.

The entire MMC chip is mounted and conductively connected to a large Faraday-Cup by screws and additionally secured by conductive copper tape. The installation within the RISIKO implantation and Faraday cup assembly is shown in the photos of Fig. 2, which are recorded with and without the aperture slit, and which are showing the individual MMC pixels visible as small spots centrally within the slit in both cases. For preventing any contribution in the implanted sample, which might stem from memory effects or cross contaminations from earlier studies and implementations performed at RISIKO, the components of the collection Faraday cup are regularly inspected for their activity level and frequently exchanged. High sensitivity studies of removed components at low level counters have never showed any relevant activity above background collected therein, which would affect the upcoming implantation process.

The ^{55}Fe sample is prepared as an HNO_3 solution of which 1 µL contains $3 \cdot 10^{13}$ ^{55}Fe atoms. Individual samples of $1.2 \cdot 10^{14}$ ^{55}Fe atoms, corresponding to the German exemption limit of 1 MBq, are extracted and directly dropped into the atomizer cavity. Therein the solution is dried for several hours under a heat lamp at the Department of Chemistry – TRIGA site before delivery to the RISIKO lab of Mainz University.

2.1. Resonance ionization of ^{55}Fe

For efficient ionization of ^{55}Fe, we use a recently identified and precisely characterized two-step optical excitation/ionization scheme for iron, which is shown in Fig. 3a. For the first excitation step, which populates the 39 625.8 cm^{-1} state along the strong 3 d^6 $4s^2$ $^5D \rightarrow 3$ d^6 4s 4p $^5D^o$ transition (transition rate $2 \cdot 10^8$ s^{-1}) at 252.3 nm, third harmonic generation of the fundamental Ti:Sa laser radiation is used (Kramida et al., 2023). The intrinsic laser line width along with Doppler broadening within the atomizer results in a broad and slightly asymmetric Gaussian shape of the resonance curve, as shown in Fig. 3b. A second Ti:Sa laser, operating with intra-cavity second harmonic generation at 414.6 nm induces efficient ionization through population of the autoionizing state at 63 746.0 cm^{-1}, located well above the ionization potential of $IP_{Fe} = 63\,737.7$ cm^{-1}. In this transition, continuum interaction leads to an asymmetric Fano-profile above the ionization potential (Fano, 1961), as visible in Fig. 3c.

To verify the suitability of the excitation scheme with the available laser power, saturation curves were measured in both transitions. They are given in Fig. 4a for the first excitation step and Fig. 4b for the ionization step. Saturation is achieved at about 3 mW laser power in the first and 250 mW in the second step, which in both cases is by far surpassed by the accessible power levels.

During the preparatory phase, tests of the ionization efficiency and transmission of the mass separator in the iron mass range were conducted. For these measurements, 10^{15} atoms of stable ^{56}Fe, provided in the form of 1 µl of a commercially available diluted nitric-acid AAS standard solution with 0.2% accuracy, were prepared and introduced to the atomizer. During gradual heating of the atomizer up to complete consumption of the sample, the integration of the collected ion current on the calibrated Faraday cup, FC1 at Fig. 1, gives a precise value of the overall efficiency. The width of the slit in the focal plane was optimized on the ratio of signal-to-neighbouring-mass-suppression with transmission well above 90 %. A typical measurement of about 4 h duration including all preparations is visualized in Fig. 5. The atomizer temperature (top) and laser ion current on mass 56 (blue trace in Fig. 5b) are shown as function of time with the increasing overall efficiency indicated on the right-hand side of the graph (green line). By regularly blocking the lasers, the background contribution can be determined and subtracted, already showing the high selectivity of the laser ionization process of about 4 orders of magnitude for the isobars. The sample is heated with the power ramped up to about 400 W over about 1 h. After this point, the efficiency curve flattens but keeps still raising slightly. This is explained by two reasons: firstly, the final residuals of the sample get vaporized and secondly, the contaminations with stable iron start to contribute to some amount. These contaminations cannot be fully eliminated because all metal components of the ion source are contaminated with iron. Despite careful pre-conditioning of the ion source involving a day of heating above 400 W coupled with laser ionization, some iron contaminations still are present. Correspondingly, this background could not be reduced below 50 pA which is considered in the data analysis as background for a conservative estimation of the

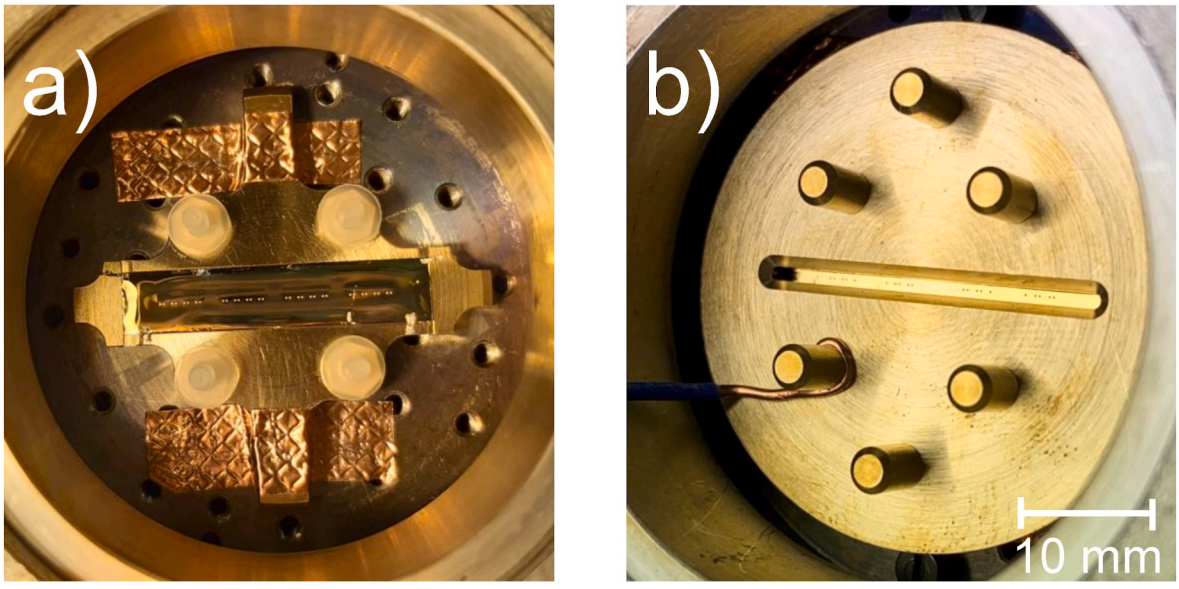

Fig. 2. Arrangement of the MMC chip within the final collection Faraday cup of RISIKO. a): Chip before aperture installation. b): Insulated aperture shielding the chip below.

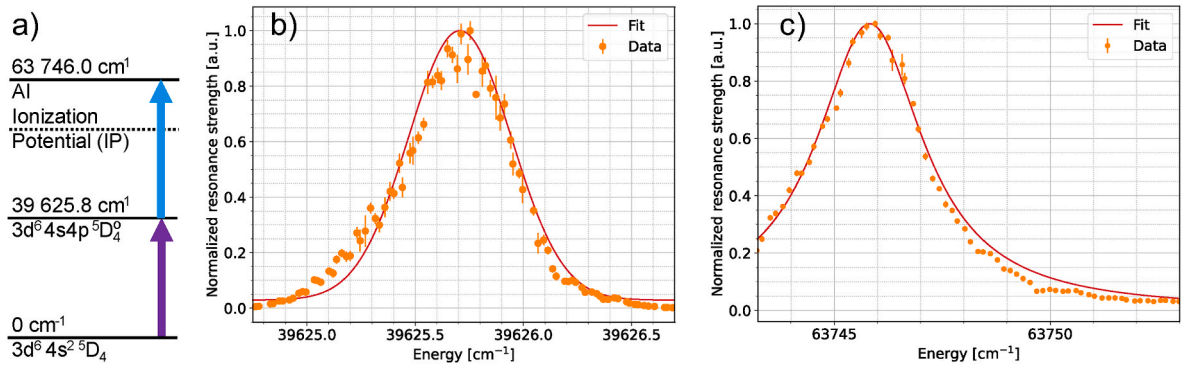

Fig. 3. a): Two-step ionization scheme for iron. b): Resonance curve and Gaussian fit of the first excitation step, realized by third-harmonic generation of Ti:Sa laser radiation at 13 208.6 cm^{-1}. c): Second step leading to a strong autoionizing state, induced by frequency doubled Ti:Sa laser light showing a Fano profile.

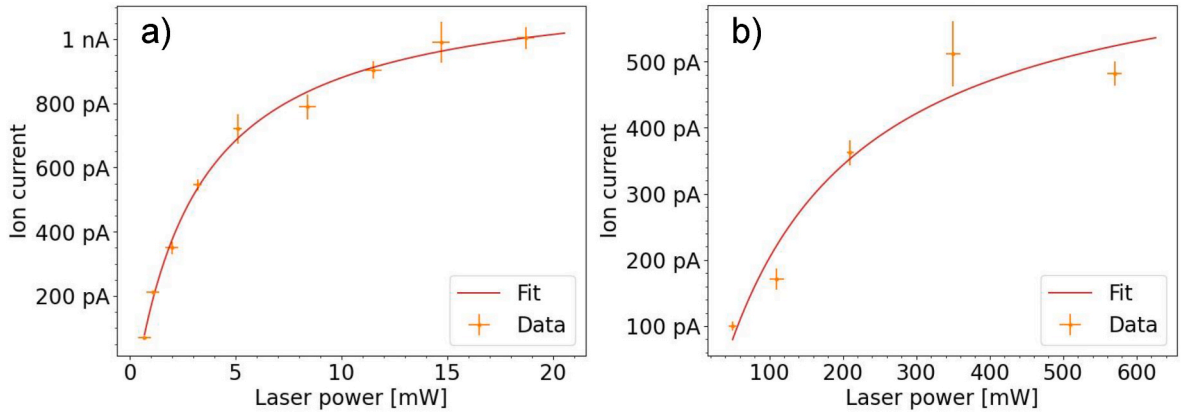

Fig. 4. Saturation curves for a): the first excitation step, b): the ionization step.

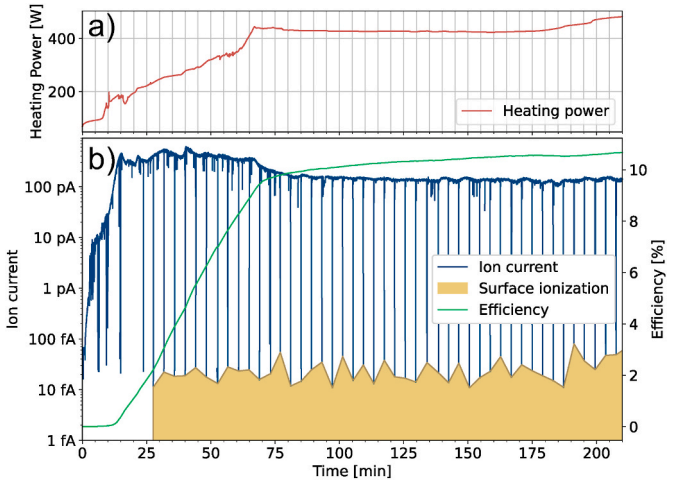

Fig. 5. Efficiency measurement showing the atomizer temperature (red trace in panel a)) and the collected ion current of ^{56}Fe (blue trace in panel b)) as function of time during the measurement. The surface ionization background is determined by regularly blocking the lasers and the overall efficiency (light green trace in panel b)) is derived by integrating the signal over time. (For interpretation of the references to colour in this figure legend, the reader is referred to the Web version of this article.)

implantation efficiency. Nevertheless, overall ionization and transmission efficiencies well above 10 % were demonstrated using a calibrated Faraday-cup.

A further relevant preparatory investigation concerns the selectivity of the implantation process regarding suppressions of the unavoidable large surplus of the neighbouring stable iron isotopes ^{54}Fe and ^{56}Fe. The ^{55}Fe sample solution was studied and showed rather high concentrations, which did not agree to natural abundances of 5.8 % and 91.8 %, respectively, but showed a strong enrichment of ^{54}Fe by a factor of about 400, which was somewhat unexpected but could explained as necessary for the breeding process of ^{55}Fe. A typical mass spectrum of the ^{55}Fe solution is shown in Fig. 6, exhibiting intense ion beams on mass 54 and mass 56 and the weak contribution of ^{55}Fe on mass 55. The unavoidable high beam currents on these neighbouring stable iron isotopes limited the ^{55}Fe ion current for implantation to 20 pA, which was already associated with about 100 nA on mass 54. At this value space charge

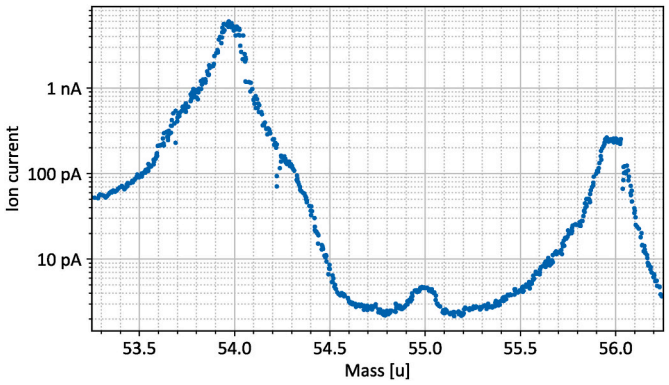

Fig. 6. Mass spectrum on the ^{55}Fe solution, exhibiting a high surplus of the stable isotopes ^{54}Fe and ^{56}Fe. Suppression of contributions on mass 55 down to 100 fA is achieved by the dispersion of the RISIKO mass separator.

effects start to affect the focalization and ion beam transmission of the RISIKO facility, which would have impaired the implantation quality for higher beam intensities. An abundance sensitivity in the suppression of these neighbouring mass contributions of more than 4 orders of magnitude towards the dominant ^{54}Fe at its high mass side and about 2 orders of abundance sensitivity of ^{56}Fe at the low mass side was demonstrated, nevertheless ensuring sufficiently clean implantation conditions on mass 55. The specific composition and contaminations contained within the ^{55}Fe sample are unknown and hence, a lowered efficiency of the actual sample has to be expected. The efficiency is not actually measured due to the limited amount available which was fully used up for implantation.

3. Implantation procedure

Well controlled and quantified implantation of ^{55}Fe into the arrangement of MMCs is achieved by strong focalization and precise positioning of the ion beam onto the chip surface and applying proper scanning by the deflectors in X- and Y-direction via a computer routine. The electronic read-out of the ion current on the chip can be used for a two-dimensional image of the implantation area, which is defined by the aperture with its central slit of 24 mm according to the arrangement shown in the photo of Fig. 2b.

Fig. 7a shows low resolution scanning of 100 V/step, corresponding to a movement of 120 µm/step while the ion current on the chip on FC2 is read out. The visualization of these data is showing the grounded aperture in a blueish colour of low values while the chip as well as the edges of FC2 are shown in yellowish for high currents measured. The scan voltages chosen permit for wide area scanning in a reasonable measuring time to map the entire area of the collection Faraday cup. A higher resolved scan over the implantation region of the absorber area, situated behind the slit, taken with step size of 25 V corresponding to 30 µm/step is given in Fig. 7b. This data is used for proper setting of the scan range in the computer routine. Due to imperfect suppression of sputtered electrons and ions in this large area Faraday cup, the current readout in these measurements is neither exact nor linear in intensity and thus not suitable for precise ion beam quantification. Accordingly, this value is regularly calibrated during the implantation process by interspersed current measurements at the retractable and calibrated FC1.

As it has been studied in detail in (Kieck et al., 2019) for the implantation of ^{163}Ho on MMC chips, a weak ion current well below 0.2 nA has proven ideal for good focalization with circular beam spot size of about 0.5 mm diameter of Gaussian shape (FWHM). This size could be verified for the case of iron, for which an even weaker current of only 20 pA has been chosen to account for possibly stronger influences of contaminations in the sample, obstructing the ion beam formation at the ion source and along the ion beam path before the magnet. With this setting an implantation run of ^{55}Fe takes about 3 h up to complete consumption of the sample. The sequence of a typical implantation procedure thus includes the steps:

1. Initial optimization of the laser ionization process and the mass separator setting, performed on stable ^{56}Fe, which is extracted from the ion source at low heating temperatures to avoid notable losses of the ^{55}Fe atoms in the sample.
2. Mass separator tuning to mass 55 and ion beam quantification measurements on FC1 at the start of the implantation and interspersed each 2 min.
3. Controlled increase of the atomizer temperature up to reaching the chosen ion beam intensity of about 20 pA, which ensures high spatial beam quality.
4. High resolution scan across the predefined absorber area of the MMC with typically step size of X- and Y-Deflector of 15 V, corresponding to a spatial resolution of 20 µm.
5. Gradual heating of the atomizer for stabilization of the ion-beam current around 20 pA and going back to step 3 up to exhaustion of the sample.

The total number of implanted atoms is obtained from the integration of the ion current, which was measured on the calibrated Faraday cup in intervals of about 5 min and stepwise linearly interpolated between those measurements over the entire implantation time. Fig. 8 documents one of the measurements over a full implantation procedure, showing a smooth implantation with an ion current kept between 15 pA and 22 pA during the entire duration of more than 2 h. A drop of the current below 3 pA at maximum atomizer temperature of 2000 K was considered as empty source and the implantation procedure was

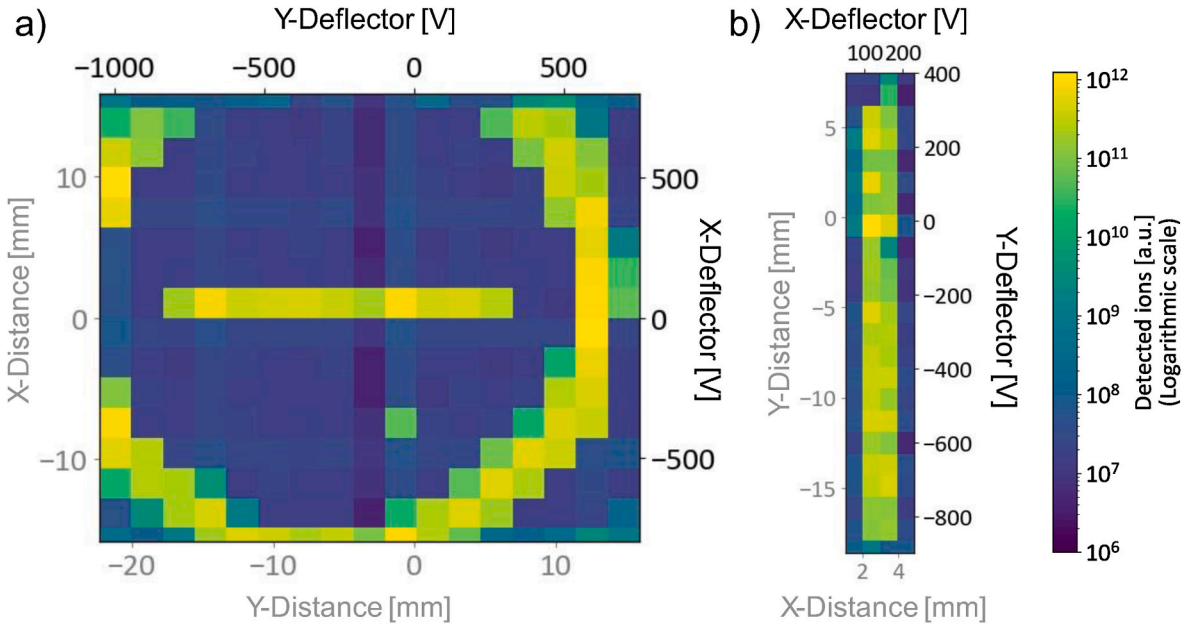

Fig. 7. Scan of the implantation area. The aperture is grounded, while the MMC chip is read out through the Faraday-Cup. Deflector voltages and actual deflections at the implantation site in both axes are given. a): Two-dimensional low-resolution mapping of the aperture with horizontal slit and a narrow circular ring around the aperture b): Higher resolved scan over the central slit used for setting the scan range. Figure rotated by 90°.

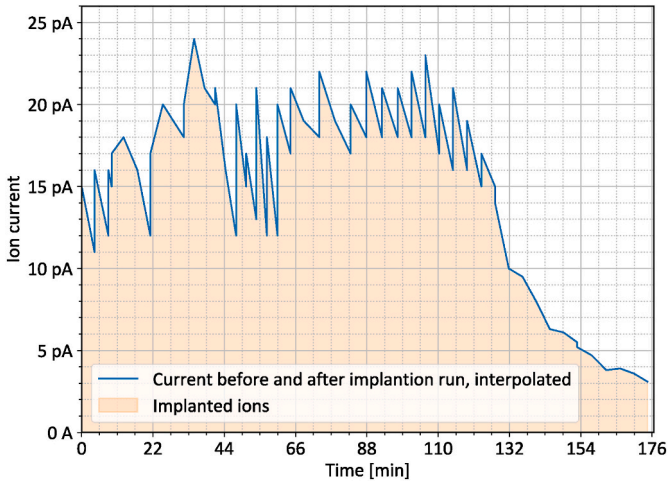

Fig. 8. Documentation of the ion beam current during implantation of 4.2 Bq of ^{55}Fe into each MMC pixel of one of the chips. Measurements are taken about every 5 min before and after step-wise temperature increase of the atomizer for keeping the ion beam current at the desired value of about 20 pA.

stopped. This routine operation description was used for all implantation runs following the first test implantation. The measurement shown in Fig. 8 resulted in 4.2 ± 1.1 kBq implanted on the chip and nearly twice as much on the aperture, corresponding to about 4 Bq per absorber.

3.1. Implantation results

In total, 11 commercially purchased samples of ^{55}Fe with $1.2 \cdot 10^{14}$ atoms, corresponding to 1 MBq each, were used to implant five different MMC chips, each containing 32 absorbers. Following a first test implantation experiment, this MMC chip, together with its holder and aperture shield, was shipped to PTB Braunschweig, Germany to determine the implanted activity and its distribution along the sample area.

The activity measurement was realized using a windowless, multiwire proportional counter, operated at atmospheric pressure with P10 argon-methane as counting gas mixture. As a first step, the detection efficiency for ^{55}Fe was derived using a simple drop-deposited point source with known activity. During the measurement, the counting threshold was set at the channel corresponding to the 1/10 of the peak position of the K X-ray peak of ^{55}Mn in the spectrum, e.g. at about 0.6 keV. With this setting, an overall detection efficiency of 24% was achieved for the drop-deposited calibration source.

In case of the implanted absorber chip, nevertheless, this value should be only seen as an upper limit on the maximum achievable counting efficiency. Since most of the activity is located some tens of nm deep in the sample material, the resulting average efficiency is expected to be somewhat lower than this. Normally, a detailed simulation of the source configuration would have been required to perform a precise efficiency transfer between the drop-deposited and the implanted source

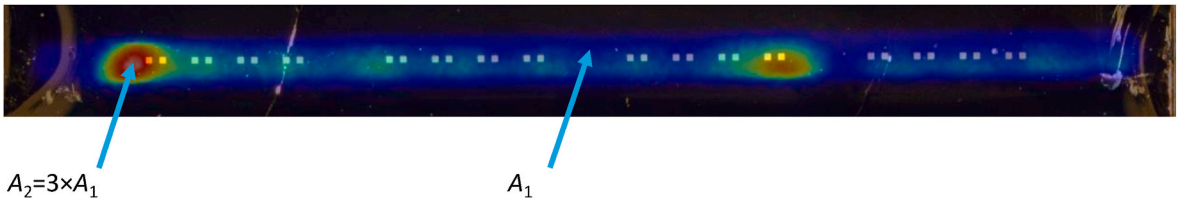

Fig. 9. Activity distribution on the test chip with an average activity of 0.7 Bq. The hot spots in red – caused by artefacts of the implantation routine – have an activity about three times higher than the blue areas. (For interpretation of the references to colour in this figure legend, the reader is referred to the Web version of this article.)

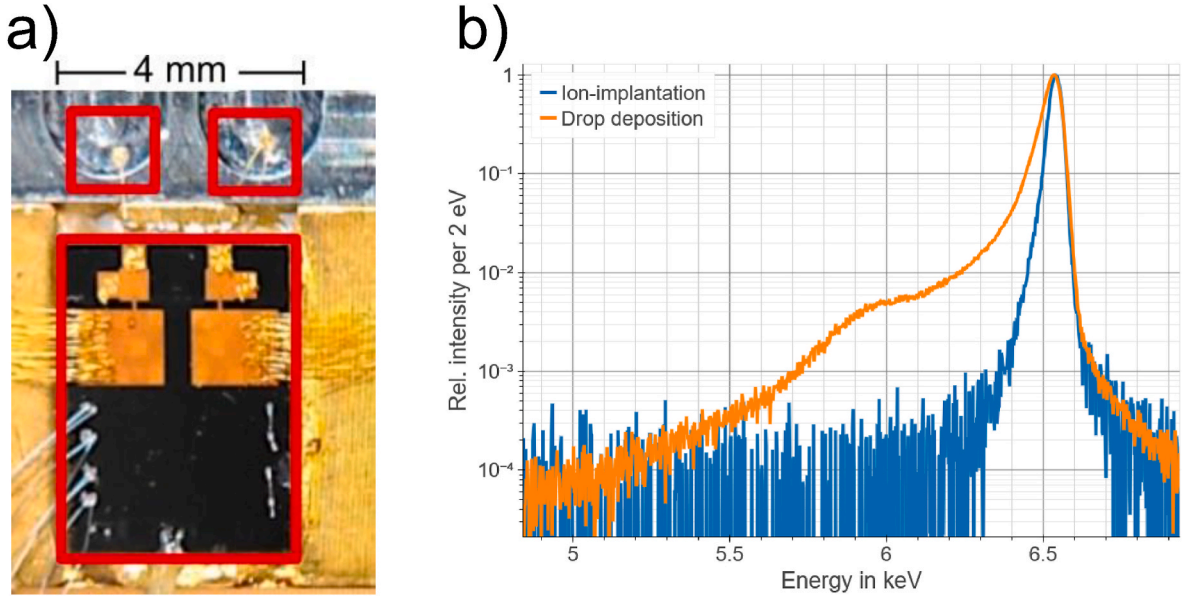

Fig. 10. Left) Photo of implanted absorbers (top red squares) thermally coupled by bond wires to the MMC chip (bottom red square). Right) Decay energy spectrum of the EC of ^{55}Fe. The spectra are normalized to the maximum intensity of the K binding energy of Manganese. The spectrum plotted in orange corresponds to a drop-deposited source while the blue one corresponds to an ion-implanted source. In both cases no background is subtracted. (For interpretation of the references to colour in this figure legend, the reader is referred to the Web version of this article.)

geometry. However, since the activity measurement is only meant to serve as a qualitative benchmark for the implantation process, for the present purpose it was sufficient to place a conservative estimate of (20 ± 5) % on the efficiency.

Based on the measurements with the windowless proportional counter, the total implanted activity in the first test implantation on a MMC chip amounted to approximately 1 kBq, while about twice as much activity was deposited into the material around the aperture.

The distribution of ^{55}Fe atoms in the surface of the MMC chip was studied using a commercial autoradiography system. For this purpose, the MMC chip, still mounted in the irradiation holder, was placed on a digital imaging plate with the implanted surface facing downwards. In addition, an anodized, large area ^{241}Am source with active area of 10 × 10 cm^2 was positioned on top of the MMC chip. This was done to obtain a clear outline of the sample holder, which could be later be used to precisely overlay the intensity distribution from autoradiography on the optical image of the chip (see Fig. 9) and a subsequent autoradiography without the Americium source. This could be done accurately using the implanted absorbers as reference points. The presence of the ^{241}Am source did not disturb the measurement, because the part of the imaging plate in contact with the MMC chip was shielded by the copper of the sample holder from the radiation originating from the ^{241}Am source, and thus this area of the film was only exposed by the ^{55}Fe implanted in the chip.

The result of the autoradiography confirmed the specified overall ion beam width of 0.5 mm. Moreover, the general precision of hitting the extended absorber area of 20 mm length could be proven. Nevertheless, a slight vertical displacement of the center of the implantation region of about 0.2 mm size in respect to the axes of the absorbers is evident from the image. It was caused by minor imprecisions and possible scan to scan instabilities of setting and controlling the deflector voltages. Due to the beam size of 0.5 mm, deviations on this scale are difficult to avoid at the RISIKO facility in its present development state.

Overall, a rather homogeneous deposition of activity has been obtained, except for the two well visible hot spots (shown in red) at the left edge and at the end of the 4th block of absorbers. By combining the result of the activity measurement with the relative intensity distribution obtained from autoradiography, the average deposited activity per absorber in this measurement was estimated to be about 0.7 Bq. The two hot spots show activity levels which exceed this average by a factor of 2–3, respectively. They are caused by artefacts of the initial automated implantation routine, which started at one of the points, regularly jumping back to there for spatial calibration and stopped at the other, in this way overloading these spots.

The above-described results were used to optimize the implantation procedure for the following campaigns. Thanks to this effort, the loaded activity per MMC pixel could be increased considerably. Two out of the four MMC chips delivered to the EU-EMPIR project PrimA-LTD consortium for testing and subsequent application had an average activity per pixel of 4.2 ± 1.1 Bq. In case of the third and fourth chip arrays, the absorbers received activities of 5± 1.2 Bq and 3.5± 1.1 Bq, respectively. We have refrained from further autoradiography measurements in order to reduce any risk of destroying the implanted chips.

After initial characterisation of the test chip following implantation, the micro fabrication was finalized by electroplating the second gold layer on top of the absorbers to fully enclose the ^{55}Fe. To perform decay energy spectrometry, the individual absorbers with a pixel size of 170 μm × 170 μm were detached from the chip using a razor blade and glued onto an aluminium holder (Fig. 10a). The measurements were performed using RoS type M MMCs, which were developed within the PrimA-LTD project (Müller et al., 2024), and 2-stage PTB dc-SQUIDs of the type C6S116W in a dilution refrigerator operated at 10 mK. Data was analysed as described in (Szymkowiak et al., 1993; McCammon, 2005; Paulsen et al., 2024) using an energy calibration based on Williams (2009). As only a negligible contamination of ^{60}Co with an activity ratio well below 10^{-4} relative to ^{55}Fe was found, the resulting spectrum was zoomed onto the K binding energy of Manganese. Data for the ion-implanted sources is shown in blue in Fig. 10b. While the energy resolution does not differ too much from the absorbers made by drop deposition the peak shape drastically improves. Mainly Auger electrons losing energy in the crystal structure of the dried residue cause a low energy tailing for drop-deposited sources because the heat transfer is on a different timescale reducing the detected decay energy. On the other hand, the implanted absorbers show a nearly symmetrical Gaussian shape because of a uniform thermalisation in the gold absorber. It should be noted that the abovementioned combination of MMC and SQUID types is far from optimal and serves only as a first benchmark to show the superior spectrum quality of implanted sources. The energy resolution is expected to improve significantly once the measurement of the fully integrated source-MMC setup is carried out.

4. Conclusion and outlook

The implantation of the radioisotope ^{55}Fe into the MMC chips in the framework of the EMPIR project has successfully been carried out at the RISIKO laser mass spectrometry facility of Mainz University. Four chips with activity levels close to the optimum value of 5 Bq per detector pixel were prepared and one test chip with 0.7 Bq per pixel was investigated by autoradiography proving the outcome and quality of the implantation process. Preparatory measurements on the resonant laser ionization process have provided deeper insights into the atomic spectrum of iron and delivered necessary information for the implantation at RISIKO via RIMS. The atomization process of the sample could be optimized regarding overall efficiency, purity of the ion beam and spatial quality of the beam to permit for this demanding application. The implanted chips are undergoing tests and calibration measurements within the labs of the EMPIR PrimA-LTD consortium. Initial preliminary results suggest better performance than drop-deposited chips.

CRediT authorship contribution statement

Thorben Niemeyer: Writing – review & editing, Writing – original draft, Software, Methodology, Data curation, Conceptualization. **Daniel Mowitz:** Software, Methodology, Data curation. **Sebastian Berndt:** Supervision, Methodology, Data curation. **Jörn Beyer:** Project administration, Funding acquisition, Conceptualization. **Holger Dorrer:** Data curation. **Christoph E. Düllmann:** Writing – review & editing, Supervision. **Alexander Göggelmann:** Writing – original draft, Methodology, Data curation. **Raphael Hasse:** Data curation. **Sebastian Kempf:** Supervision, Project administration, Funding acquisition. **Tom Kieck:** Supervision. **Nina Kneip:** Supervision, Project administration, Data curation, Conceptualization. **Karsten Kossert:** Writing – original draft, Supervision, Project administration, Funding acquisition, Conceptualization. **Andrea T. Loria Basto:** Data curation. **Christoph Mokry:** Data curation. **Michael Müller:** Resources, Methodology, Data curation. **Ole J. Nähle:** Writing – review & editing, Supervision, Project administration, Funding acquisition, Conceptualization. **Dennis Renisch:** Writing – review & editing, Supervision, Project administration, Funding acquisition, Conceptualization. **Jörg Runke:** Data curation. **Dominik Studer:** Supervision, Project administration, Conceptualization. **Marcell P. Takács:** Methodology, Data curation. **Klaus Wendt:** Writing – review & editing, Writing – original draft, Supervision, Resources, Project administration, Funding acquisition, Conceptualization.

Declaration of competing interest

The authors declare that they have no known competing financial interests or personal relationships that could have appeared to influence the work reported in this paper.

Acknowledgements

This project, 20FUN04 PrimA-LTD, has received funding from the EMPIR program co-financed by the Participating States and from the European Union' s Horizon 2020 research and innovation program.

Data availability

Data will be made available on request.

References

Bobin, C., Thiam, C., M'Hayham, M.-D., Mougeot, X., 2023. Activity standardization of ^{60}Co and ^{106}Ru/^{106}Rh by means of the TDCR method and the importance of the beta spectrum. Appl. Radiat. Isot. 201, 110993.

Broda, R., Cassette, P., Kossert, K., 2007. Radionuclide metrology using liquid scintillation counting. Metrologia 44, S36–S52.

Broda, R., Bonková, I., Capogni, M., Carconi, P., Cassette, P., Coulon, R., Courte, S., De Felice, P., Dziel, T., Fazio, A., Frechou, C., Galea, R., García-Toraño, E., Kolakowskal, E., Kossert, K., Krivosík, M., Lech, E., Lee, K.B., Liang, J., Listkowska, A., Liu, H., Navarro, N., Nähle, O.J., Nowicka, M., van Rooy, M., Sabot, B., Saganowski, P., Sato, Y., Tymiński, Z., Yunoki, A., Zhang, M., Ziemek, T., 2021. The CCRI(II)-K2.Fe-55.2019 key comparison of activity concentration measurements of a ^{55}Fe solution. Metrologia 58 (1A Techn. Suppl. l), 06010.

Fano, U., 1961. Effects of configuration interaction on intensities and phase shifts. Phys. Rev. 124. https://doi.org/10.1103/PhysRev.124.1866.

Gastaldo, L., et al., 2017. The electron capture in ^{163}Ho experiment – ECHo. Eur. Phys. J.: Spec. Top. 226, 1623–1694, 2017.

Grüning, C., et al., 2004. Resonance ionization mass spectrometry of plutonium with a new solid state laser system. Int. J. Mass Spectrom. 235, 171.

Kieck, T., et al., 2019. Highly efficient isotope separation and ion implantation of ^{163}Ho for the ECHo project. Nucl. Instrum. Methods Phys. Res. A 945, 162602.

Kneip, N., et al., 2022. Separation of manganese isotopes by resonance ionization mass spectrometry for ^{53}Mn half-life determination. Eur. Phys. J. Appl. Phys. 97, 19.

Kossert, K., Nähle, O., Grau Carles, A., 2011. Beta shape-factor function and activity determination of ^{241}Pu. Appl. Radiat. Isot. 69, 1246–1250.

Kossert, K., Mougeot, X., 2015. The importance of the beta spectrum calculation for accurate activity determination of ^{63}Ni by means of liquid scintillation counting. Appl. Radiat. Isot. 101, 40–43.

Kossert, K., Marganiec-Gałązka, J., Mougeot, X., Nähle, O.J., 2018. Activity determination of ^{60}Co and the importance of its beta spectrum. Appl. Radiat. Isot. 134, 212–218.

Kossert, K., Mougeot, X., 2021. Improved activity standardization of ^{90}Sr/^{90}Y by means of liquid scintillation counting. Appl. Radiat. Isot. 168, 109478. https://doi.org/10.1016/j.apradiso.2020.109478, 2021.

Kossert, K., Loidl, M., Mougeot, X., Paulsen, M., Ranitzsch, Ph, Rodrigues, M., 2022. High precision measurement of the ^{151}Sm beta decay by means of a metallic magnetic calorimeter. Appl. Radiat. Isot. 185, 110237. https://doi.org/10.1016/j.apradiso.2022.110237.

Kossert, K., Broda, R., Cassette, P., Ratel, G., Zimmerman, B., 2015. Uncertainty determination for activity measurements by means of the TDCR method and the CIEMAT/NIST efficiency tracing technique. Metrologia 52, S172–S190.

Kramida, A., Ralchenko, Yu, Reader, J., NIST ASD Team, 2023. NIST Atomic Spectra Database (Ver. 5.11). National Institute of Standards and Technology, Gaithersburg, MD. https://doi.org/10.18434/T4W30F. https://physics.nist.gov/asd.

Loidl, M., Rodrigues, M., Censier, B., Kowalski, S., Mougeot, X., Cassette, P., Branger, T., Lacour, D., 2010. First measurement of the beta spectrum of ^{241}Pu with a cryogenic detector. Appl. Radiat. Isot. 68, 1454–1458.

Loidl, M., Rodrigues, M., Le-Bret, C., Mougeot, X., 2014. Beta spectrometry with metallic magnetic calorimeters. Appl. Radiat. Isot. 87, 302–305.

Loidl, M., Rodrigues, M., Mariam, R., 2018. Measurement of the electron capture probabilities of ^{55}Fe with a metallic magnetic calorimeter. Appl. Radiat. Isot. 134, 395–398.

Mattolat, C., et al., 2009. An all-solid-state high repetiton rate titanium:sapphire laser system for resonance ionization laser ion sources. AIP Conf. Proc. 1104, 114.

McCammon, D., 2005. Thermal equilibrium calorimeters – an introduction. In: Enss, C. (Ed.), Cryogenic Particle Detection, Topics in Applied Physics, vol. 99. Springer, Berlin, Heidelberg. https://doi.org/10.1007/10933596_1.

Mertes, F., et al., 2022. Ion implantation of ^{226}Ra for a primary ^{222}Rn emanation standard. Appl. Radiat. Isot. 181, 110093.

Mougeot, X., 2023. Atomic exchange correction in forbidden unique beta transitions. Appl. Radiat. Isot. 201, 111018.

Müller, M., et al., 2024. Magnetic microcalorimeters for primary activity standardization within the EMPIR project PrimA-LTD. J. Low Temp. Phys. 214, 263–271.

Nähle, O., 2024. PrimA-LTD. In: . https://prima-ltd.net/. Last access 27 Jan 2025.

Paulsen, M., Ranitzsch, P.C.-O., Loidl, M., Rodrigues, M., Kossert, K., Mougeot, X., Singh, A., Leblond, S., Beyer, J., Bockhorn, L., Enss, C., Wegner, M., Kempf, S., Nähle, O., 2024. High precision measurement of the ^{99}Tc β spectrum. Phys. Rev. C 110, 055503. https://doi.org/10.1103/PhysRevC.110.055503.

Pommé, S., 2022. Radionuclide metrology: confidence in radioactivity measurements, J Radioanal. Nucl. Ch. 331, 4771, 479.

Riffaud, J., Kossert, K., Takács, M.P., Chiera, N.M., Schumann, D., Studer, D., Röttger, S., Wendt, K., 2024. Determination of the activity and nuclear decay data of ^{157}Tb. Appl. Radiat. Isot. 211, 2024. https://doi.org/10.1016/j.apradiso.2024.111407.

Rotzinger, H., Linck, M., Burck, A., Rodrigues, M., Loidl, M., Leblanc, E., Fleischmann, L., Fleischmann, A., Enss, C., 2008. Beta spectrometry with magnetic calorimeters. J. Low Temp. Phys. 151, 1087–1093.

Studer, D., Schumann, D., Chiera, N., Maugeri, E.A., Kieck, T., Kossert, K., Wendt, K., 2024. Towards a precise measurement of the ^{157}Tb half-life: sample preparation using mass separation. J. Instrum. (in press).

Szymkowiak, A.E., et al., 1993. Signal processing for microcalorimeters. J. Low Temp. Phys. 93, 281–285. https://doi.org/10.1007/BF00693433.

Teigelhöfer, A., et al., 2010. Grating tuned Ti:Sa laser for in-source spectroscopy of Rydberg and autoionizing states. Hyperfine Interact. 196, 161–168.

Williams, G.P., 2009. Electron binding energies. In: Thompson, A., Vaughan, D. (Eds.), X-Ray Data Booklet. Lawrence Berkeley National Laboratory, University of California. https://xdb.lbl.go.